Plasma particle simulations on stray photoelectron current flows around a spacecraft

AUTHOR(S):

Miyake, Y.; Usui, H.; Kojima, H.; Nakashima, H.

CITATION:

Miyake, Y. ...[et al]. Plasma particle simulations on stray photoelectron current flows around a spacecraft. Journal of Geophysical Research: Space Physics 2012, 117(A9): A09210.

ISSUE DATE:

2012-09

URL:

http://hdl.handle.net/2433/193713

JOURNAL OF GEOPHYSICAL RESEARCH, VOL. 117, A09210, doi:10.1029/2012JA017673, 2012

Plasma particle simulations on stray photoelectron current flows around a spacecraft

Y. Miyake,[1] H. Usui,[1] H. Kojima,[2] and H. Nakashima[3]

Received 2 March 2012; revised 25 July 2012; accepted 28 July 2012; published 13 September 2012.

[1] In tenuous space plasmas, photoelectron flows produce complex current paths among multiple conducting elements of spacecraft, which may influence the current–voltage characteristics of double-probe electric field sensors. We performed full-particle simulations on this effect by assuming a sensor configuration that is typical of recent designs like those on Cluster, THEMIS, and BepiColombo/MMO; the spherical probe is separated from a conducting boom by biased electrodes known as the 'stub' and the 'guard'. The assumed bias potential scheme corresponds to that planned for BepiColombo/MMO and is different from those used in the other satellites. The analysis focuses on stray photoelectron currents flowing from these electrodes and a spacecraft body. Photoelectrons approaching the probe are commonly repelled by the guard, the potential of which is strongly biased negatively, and are subsequently affected by the probe potential. Consequently, the photoelectron current magnitude increases with increasing probe potential regardless of their origins, when the probe operates between the plasma and floating spacecraft potentials. The result indicates that both photoelectron currents from the spacecraft body and biased electrodes can be minimized by selecting the probe working potential as close as possible to the plasma potential. We also examine the photoelectron current dependence on the presence or absence of the guard electrode operation and confirm a positive effect of reducing the photoelectron current from the spacecraft. However, negative side effects of the guard operation enhance the photoelectron currents from the stub and guard, when the probe operates nearly at the plasma potential.

Citation: Miyake, Y., H. Usui, H. Kojima, and H. Nakashima (2012), Plasma particle simulations on stray photoelectron current flows around a spacecraft, *J. Geophys. Res.*, *117*, A09210, doi:10.1029/2012JA017673.

1. Introduction

[2] The double-probe technique is commonly used for electric field measurements in scientific space missions. Since the technique was put to practical use in early days of space exploration [*Mozer and Bruston*, 1967; *Mozer et al.*, 1976], its fundamental principles have been discussed exhaustively [*Fahleson*, 1967; *Pedersen et al.*, 1984; *Tsuruda et al.*, 1994; *Pedersen et al.*, 1998; *Gurnett*, 1998]. In these studies, it has been pointed out that the accuracy of this measurement technique is readily affected by perturbations due to surrounding plasmas. In tenuous plasma environments, such perturbations are mainly caused by photoelectron emission from sunlit surfaces of the spacecraft and sensor bodies.

[3] In the past few decades, much effort has been made to improve the double-probe technique to enhance the reliability of electric field measurements in environments with photoelectrons. One improvement that has been made is the installation of a photoelectron guard electrode. The main purpose of this electrode is to minimize undesirable influences caused by photoelectrons from the spacecraft body.

[4] A photoelectron guard electrode is used practically in the Cluster Electric Fields and Waves (EFW) instrument [*Gustafsson et al.*, 1997, 2001]. Continuous improvements were subsequently made for its use on the THEMIS Electric Field Instrument (EFI) [*Bonnell et al.*, 2008]. There are currently plans to apply the technique to the Mercury Electric Field In-Situ TOol (MEFISTO) for the BepiColombo/MMO spacecraft to Mercury [*Blomberg et al.*, 2006].

[5] The present paper investigates the current–voltage characteristics of a double-probe sensor in an environment with a high density of photoelectrons. An accurate knowledge of the current–voltage characteristics is generally necessary to determine the optimum working point of

[1]Graduate School of System Informatics, Kobe University, Kobe, Japan.
[2]Research Institute for Sustainable Humanosphere, Kyoto University, Kyoto, Japan.
[3]Academic Center for Computing and Media Studies, Kyoto University, Kyoto, Japan.

Corresponding author: Y. Miyake, Graduate School of System Informatics, Kobe University, 1–1, Rokkodai-cho, Nada-ku, Kobe 657-8501, Japan. (y-miyake@eagle.kobe-u.ac.jp)

0148-0227/12/2012JA017673

the probe. In addition, the gradient of the current–voltage characteristic curve gives the sheath conductance. The sheath conductance is a key parameter for realizing optimal sensor operations as a simple voltmeter for static fields [*Pedersen et al.*, 1998] and also for calibrating plasma wave data obtained in a very low frequency range [*Gurnett*, 1998].

[6] The current–voltage characteristics are often overly simplified by considering only photoelectron emission and plasma collection by the probe. In reality, stray photoelectron currents flowing between the probe and other conducting elements can influence the characteristics [e.g., *Pedersen et al.*, 2008]. These stray photocurrents make it difficult to estimate the current–voltage characteristics analytically; thus, some sort of numerical approaches must be used, including self-consistent modeling of the photoelectron kinetics.

[7] Consequently, we use particle-in-cell (PIC) simulations to investigate the problem. The Electro-Magnetic Spacecraft Environment Simulator (EMSES) proposed in a previous paper is based on the electromagnetic PIC algorithm combined with internal boundaries that describe the conducting spacecraft and sensor surfaces [*Miyake and Usui*, 2009]. Conceptually, EMSES provides self-consistent solutions for the plasma and photoelectron behaviors as well as the transient variation of spacecraft and sensor potentials. We mainly adopt this self-consistent approach in the present study. However, by the approach, it is impractical to treat realistic sensor dimensions within currently available computational resources. This impracticality is due to the extremely broad range of spatial scales associated with the problem. The aspect should be treated separately by making some a priori assumptions rather than by employing a self-consistent treatment. Such an approach is discussed in section 4.1.

[8] Some previous studies have investigated the sensor characteristics in photoelectron environments including the stray photoelectron effects. *Cully et al.* [2007] reported overall structures for the electric potential and the photoelectron distributions around the Cluster satellite and addressed some related field measurement problems. For Cluster, *Pedersen et al.* [2008] also studied the photoelectron current characteristics in order to use the probes as a potential reference in their spacecraft potential measurements. *Miyake et al.* [2011] examined how a guard electrode installed in some recent double-probe sensors affects the photoelectron distribution. Following on from our previous paper, we investigate stray photoelectron currents in detail by subdividing current components based on their origins. Since this is the first time that such a detailed approach has been adopted, we expect to obtain new insights that will help improve the design and use of the double-probe technique.

[9] In section 2, we describe a numerical model of the sensor and the simulation setup. Section 3 presents the simulation results for the current–voltage characteristics of an electric field sensor, focusing the effects of stray photoelectron currents. We perform photoelectron orbital analysis to clarify the behavior of photoelectrons emitted from the sensor and spacecraft elements. We also discuss the effects of a photoelectron guard electrode in this section. Section 4 is devoted to scaling analysis of stray currents for practical sensor dimensions.

2. Simulation Model

2.1. Simulation Code

[10] We use the three-dimensional plasma particle simulation tool EMSES [*Miyake and Usui*, 2009] for the self-consistent analysis of spacecraft-plasma interactions. The analysis requires appropriate inclusion of solid conducting bodies as internal boundaries and the effect of the plasma impingement and the photoelectron emission on the electric potentials of the bodies. EMSES is based on the PIC method [*Birdsall and Langdon*, 1985] and employs boundary treatments for both longitudinal and transverse electric field components at the interface between a plasma and a conducting body. All field components in EMSES are defined on a uniform Cartesian grid.

[11] Normally, the entire spacecraft system including the sensor is floating in terms of electric potential. Then, either bias voltage or current is imposed on arbitrary pairs of the spacecraft and sensor components. We simulate this potential treatment in the investigations except in section 4.1. The analysis performed in section 4.1 employs the prescribed potentials for spacecraft and sensor instead of the floating potential condition. Photoelectron emission from the surface is simulated by using a conventional particle-loading scheme [*Cartwright et al.*, 2000]. The number of emitted photoelectrons per one time step and their energies assuming a single Maxwellian are given as input parameters. More detailed descriptions about the above techniques are available in a previous paper [*Miyake et al.*, 2011].

[12] Because we solve $\sim 3 \times 10^8$ macro-particles and 128^3 grid points every time step for the present investigations, it is necessary to use a supercomputer. Hence the adaptation of EMSES to modern distributed-memory parallel computers is an important issue. We parallelized EMSES based on the domain decomposition method and implemented our original dynamic load-balancing algorithm OhHelp [*Nakashima et al.*, 2009]. Although we here avoid a lengthy explanation about the algorithm, OhHelp realizes efficient computations that are scalable in terms of both number of macro-particles and domain size. The present computations are performed using four nodes of Fujitsu's HX600 cluster each with four quad-core Opteron processors and 32 GB shared memory, which are compliant with the T2K Open Supercomputer specifications [*Nakashima*, 2008].

2.2. Electric Field Sensor Model

[13] Figure 1a illustrates the sensor model used in the present simulation. The model is relevant to the latest design of the electric field sensor for BepiColombo/MMO, and is essentially the same as that described in our preceding study [*Miyake et al.*, 2011]. Because the validity and limitations of the model are presented in the previous paper in detail, we here review the specifications of the sensor model briefly. The sensor consists of a probe, a sensor wire, a boom wire, and a preamplifier housing (referred to as a puck). One sensing element consists of a probe and a wire, the surfaces of which have the same electric potential. The boom surface is made of a conducting material and is electrically

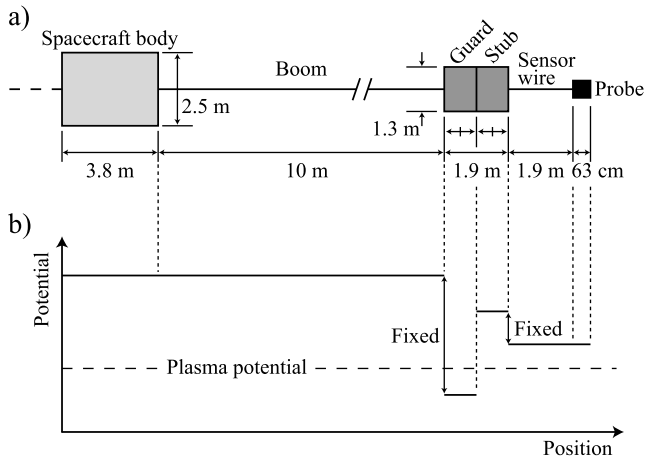

Figure 1. Numerical model of electric field sensor used in the present study. (a) Configuration and dimensions of the sensor model. The boom and the sensor wire have the shape of rectangular bars, the cross-section of which is a square, 6.3 cm on a side. (b) Typical relations among spacecraft and sensor body potentials. The guard and stub potentials are always in conjunction with those of spacecraft and probe, respectively. The floating potential of the probe is controlled actively by changing the magnitude of a bias current from the spacecraft.

connected to the spacecraft ground. The puck is installed between the sensing element and the boom.

[14] By applying certain voltages to the puck surface, the puck can also function as a photoelectron guard electrode. The puck surface consists of two parts that are electrically insulated from each other. The inner (boom-side) and outer (probe-side) surfaces of the puck are respectively referred to as the guard and the stub. We independently apply voltages to the guard and the stub such that the guard has a potential of $-8\phi_{ph}$ relative to that of the spacecraft, while the potential of the stub is $+2\phi_{ph}$ relative to the probe potential. Here, the product of ϕ_{ph} and the unit charge e corresponds to the most probable photoelectron energy. The guard electrode repels photoelectrons emitted from the spacecraft body to prevent them from approaching the probe, while the stub electrode attracts photoelectrons emitted from the probe.

[15] The bias potential scheme introduced above is relevant to that planned for the BepiColombo/MMO mission [*Blomberg et al.*, 2006]. Note that the Cluster, THEMIS, and some other spacecraft adopt a different scheme; i.e., the guard is biased relative not to the spacecraft potential but to the probe potential [*Gustafsson et al.*, 1997; *Bonnell et al.*, 2008].

[16] In addition to the voltage biasing, a current with a constant magnitude is provided as a bias current from the spacecraft body to the probe. The magnitude of this current is treated as an input parameter I_{bias} in this study. We are particularly interested in the dependence of the sensor properties on I_{bias}. The probe potential is actively controlled by I_{bias}, which determines the sensor working point on the current–voltage characteristic curve of the probe. To examine the effects of the photoelectron current at various working points, we performed multiple simulations for various input values of I_{bias}.

[17] As a result of the voltage and current biasing, we assume electric potential relations as shown in Figure 1b among spacecraft and sensor elements. This paper does not give a lengthy description of the numerical formulation for the voltage and current biasing; section 2.3 of *Miyake et al.* [2011] provides a complete description. What we should address here is that the above treatments ensure that the total charge is rigorously conserved for the entire spacecraft. Specifically, the voltage and current biasing never alters the total spacecraft charge, and only currents generated by the impingement and emission of plasma particles can alter the total charge.

[18] As discussed in a previous paper by us [*Miyake et al.*, 2011], since we represent the geometry using a limited number of rectangular grid elements, certain components will be considerably deformed from typical designs for instruments. The sensor dimensions need to be considerably larger than those of practical instruments. This deformation is most pronounced for the radii of the sensor and boom wires. Also, the deformation of the probe and puck is not negligible. Furthermore, the shapes of some sensor elements differ from those of practical elements (e.g., the probe is spherical and the boom is cylindrical typically). Considering these limitations, the simulation outputs need to be treated with great caution; this problem is discussed in section 4.1. Some previous studies have effectively addressed this problem by limiting their applicability to very tenuous plasma environments [e.g., *Cully et al.*, 2007]. However, the present study does not consider combining their techniques with the present approach due to the technical difficulties in doing this.

2.3. Simulation Setup

[19] Figure 2 shows the three-dimensional simulation setup. We place the spacecraft body with a pair of electric field sensors aligned with the z-axis in the three-dimensional simulation box. The box is filled with background plasma composed of electrons and protons with finite thermal velocities, the Debye length λ_D of which is set to ~1/10 times the box size on each side. We assume that the sun illuminates the spacecraft body and the sensors from the $+x$

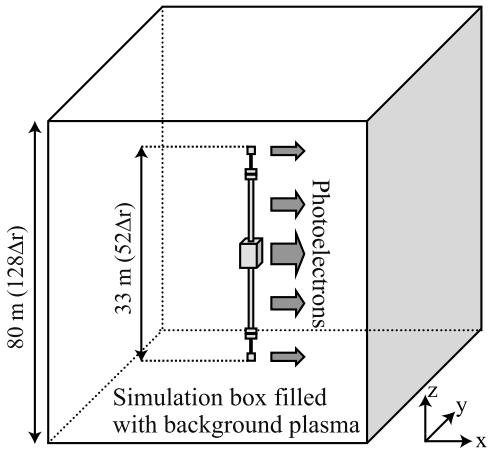

Figure 2. Three-dimensional simulation setup used in the present analysis.

Table 1. System, Background Plasma, and Photoelectron Parameters Considered in the Present Analysis

Parameter	Value
System	
Grid spacing	6.3×10^{-1} m
Time step width	2.4×10^{-1} μs
System length	80 m
Background plasma	
Number density	8.5 cc^{-1}
Electron and ion temperatures	10^5 K
Debye length	~7.5 m
Electron differential current density	6.7×10^{-7} Am^{-2}
Photoelectron	
Current density	1.7×10^{-5} Am^{-2}
Energy	2.2 eV

direction. The boundary conditions for the outer edges of the simulation box are selected to give an isolated system [*Miyake et al.*, 2008]. We employ the Dirichlet condition for the outer boundary values of the electrostatic potential. We also inject particles with the same properties as the background plasma from the boundaries to supplement particles escaping from the simulation box.

[20] Table 1 lists the principal plasma parameters used in the present simulations. In this study, we seek to simulate a ubiquitous tenuous plasma environment to clarify the general aspects of photoelectron effects. As will be seen from the simulation results, the parameter set produces a photoelectron population that is denser and colder than the background plasma. The resulting photoelectron shielding length is much shorter than both the sensor tip-to-tip length and the Debye length λ_D of the background plasma.

[21] We exclude any effects of the secondary electron emission from the simulation model. The secondary emission is generally important when a primary electron energy ranges from several tens of eV to a few keV depending on the surface material [*Lai*, 2011]. In the present situation, both photo- and background electron energies are sufficiently low compared to this energy range, and thus the secondary electron yield would not be appreciable. Further, even if a small amount of secondary electrons is emitted, the secondary electrons usually have only a few eV in energy. This implies that the emitted secondary electrons should be mostly attracted back due to the positive spacecraft potential and will not contribute substantially to the net current. Thus we choose to exclude the effect here.

[22] The other conditions are determined as follows. The mass ratio of an electron–proton background plasma is taken to be its actual value, namely $m_i/m_e = 1836$, where m_e and m_i represent the electron and proton masses, respectively. The background electron and ion temperatures, T_e and T_i, respectively, satisfy an isothermal condition (i.e., $T_e = T_i$). In the present study, there is no static magnetic field in the simulation box. In the outer magnetospheric plasma, the electron gyroradius is generally longer than the sensor tip-to-tip length even for photoelectrons, and practical influence of the static magnetic field on the photoelectron behavior is assumed to be presumably small. We will revisit the issue in section 4.2 to verify this assumption.

3. Simulation Results

3.1. Current–Voltage Characteristics

[23] This paper investigates the current–voltage characteristics of the sensor, which reflect the nature of plasma and photoelectron currents around the probes. For this, we perform a series of simulations for several values of I_{bias} and measure the equilibrium probe potential ϕ_{pr} in a floating condition. The floating probe potential is determined such that the following current balance condition is satisfied:

$$I_{ph}(\phi_{pr}) + I_{se}(\phi_{pr}) + I_e(\phi_{pr}) + I_i(\phi_{pr}) + I_{stray}(\phi_{pr}) + I_{bias} = 0, \quad (1)$$

where I_{ph}, I_{se}, I_e, and I_i are functions of ϕ_{pr} and correspond to the photoelectron and secondary electron currents emitted by the probe, and the background electron and ion currents, respectively. The term I_{stray} indicates the stray current due to photoelectron flow between the probe and other conducting elements. Note that I_{ph} is defined here as a current delivered by photoelectrons that are not trapped by any conducting elements (including the probe itself and other elements) and escape into the background space eventually. All the currents in equation (1) are defined such that they are positive when positive charge is accumulated at the probe. Recalling that we assume $I_{se} = 0$ as described in section 2.3, equation (1) can be rewritten as $I_{bias} = -(I_{ph}(\phi_{pr}) + I_e(\phi_{pr}) + I_i(\phi_{pr}) + I_{stray}(\phi_{pr}))$, which indicates that the magnitude of I_{bias} is identical to that of the total current I_p delivered by charged particles flowing into and out of the probe. Consequently, we can obtain a current–voltage characteristic curve by plotting I_{bias} against ϕ_{pr}.

[24] Figure 3 displays the characteristic curve for $-I_p$ (i.e., I_{bias}) plotted against ϕ_{pr}. The obtained curve exhibits different behaviors in the two potential ranges of $\phi_{pr} < 0$

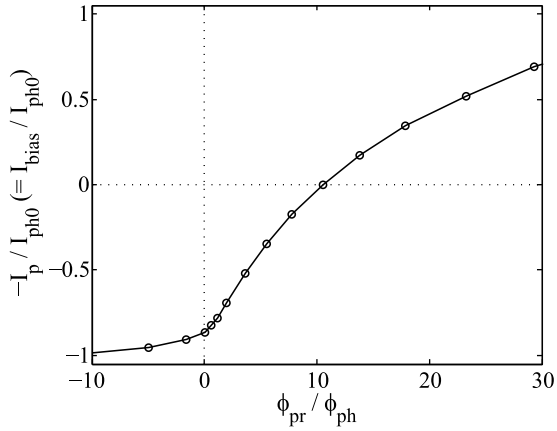

Figure 3. Current–voltage curve for a sensing element consisting of a probe and a wire. The background plasma potential is set to the reference (zero) potential. The vertical axis is normalized by I_{ph0}, which is the photoemission current in absence of recollection by any conducting elements.

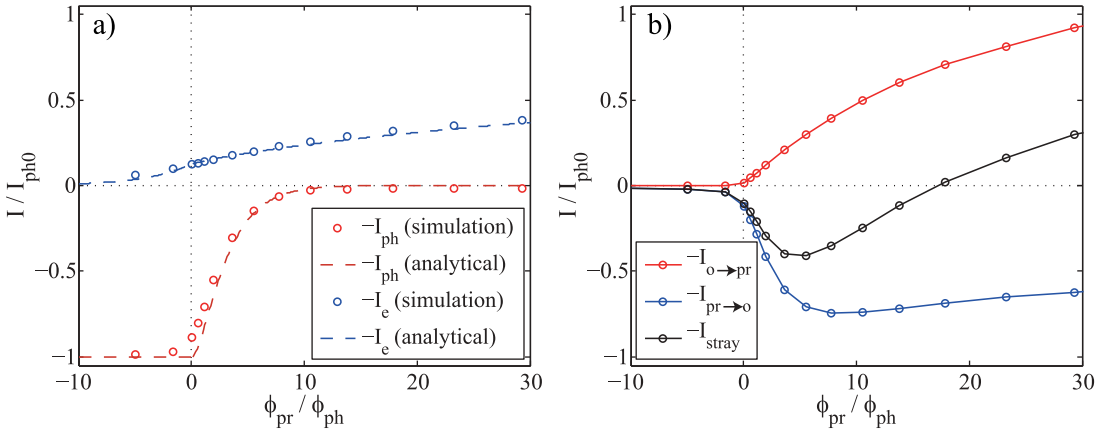

Figure 4. Current–voltage curves plotted separately for current components. (a) Characteristics of the photoemission current $-I_{ph}$ and the background electron current $-I_e$ plotted with red and blue circles, respectively. The dashed lines represent the characteristic curves evaluated using an analytical approach. (b) Characteristic curves for the stray photoelectron current between the probe and other conducting elements. The red and blue lines represent $-I_{o\rightarrow pr}$ and $-I_{pr\rightarrow o}$ respectively indicating the stray current flowing into the probe from other conducting elements besides the probe and that flowing in the opposite direction. The black line is the total stray current $-I_{stray} = -I_{pr\rightarrow o} - I_{o\rightarrow pr}$.

and $\phi_{pr} \geq 0$. For $\phi_{pr} < 0$, the curve shows a relatively moderate change and asymptotically approaches -1 with increasing $|\phi_{pr}|$. This indicates that $I_p \rightarrow I_{ph0}$ for $\phi_{pr} \ll 0$ because I_i is negligibly small in the potential range considered. Here, I_{ph0} represents the photoemission current in absence of recollection by any conducting elements. On the other hand, $-I_p$ increases drastically with increasing ϕ_{pr} in a positive potential range, while the growth rate becomes moderate as ϕ_{pr} increases. The behavior of the curve in this potential range reflects the dependence of I_{ph}, I_e, and I_{stray} on ϕ_{pr}, which is studied in more detail later.

[25] One advantage of the particle simulation approach is that conceptually all the trajectories of macro-particles inside the simulation region can be traced. We can thus obtain complete information about the composition of I_p. Figure 4 shows plots of $-I_{ph}$, $-I_e$, and $-I_{stray}$ against ϕ_{pr}. I_i is not shown in this figure because it is found to be negligibly small in this situation. In Figure 4b, the stray current is further split as $-I_{stray} = -(I_{o\rightarrow pr} + I_{pr\rightarrow o})$. Here, $I_{o\rightarrow pr}$ and $I_{pr\rightarrow o}$ are defined as the current formed by photoelectrons emitted by other conducting elements besides the probe and impinging onto the probe, and that emitted by the probe and impinging on other conducting elements, respectively.

[26] Figure 4 clearly shows that I_{ph} dominates over the other current components for $\phi_{pr} \leq 0$. For $\phi_{pr} > 0$, the contribution of I_{ph} decays with increasing ϕ_{pr} while the contributions of I_e and I_{stray} become prominent. The $-I_{stray}$ curve exhibits peculiar behavior for $\phi_{pr} > 0$ due to competition between $I_{o\rightarrow pr}$ and $I_{pr\rightarrow o}$ contributions. More in-depth analysis is done in the subsequent section to better understand the behaviors of $I_{o\rightarrow pr}$ and $I_{pr\rightarrow o}$.

[27] Of I_{ph}, I_e, and I_{stray}, the behaviors of I_{ph} and I_e can be expressed by an analytical formula by applying a conventional theory [e.g., *Mott-Smith and Langmuir*, 1926]. Although our major interest is on the I_{stray} behavior, it is also helpful to evaluate how consistent the simulation results on I_{ph} and I_e are with the theoretical evaluation. In Figure 4a, we superimpose analytical current–voltage curves for I_{ph} and I_e. These curves are calculated by considering an analogy to an emissive (electron-emitting) probe [*Hershkowitz*, 1989].

[28] The overall trends of both I_{ph} and I_e obtained in the present simulation are consistent with the simple theory, except that there is ~10% difference in I_{ph} nearly at the zero probe potential. This difference is understood by reminding the rigid definition of I_{ph} described earlier. By the definition, I_{ph} is delivered by photoelectrons that are not trapped by any conducting elements (including the probe itself and other elements) and escape into the background space eventually. Hence, the ~10% shortage of I_{ph} observed in the simulation indicates that some portion of the emitted photoelectrons is trapped by some conducting elements even at the zero potential. In this particular case, the stub electrode is reasonably identified as such a photoelectron-collecting conductor, because the stub potential is $+2\phi_{ph}$ relative to the probe. This interpretation is also consistent with the $I_{pr\rightarrow o}$ curve shown in Figure 4b, which clearly indicates the presence of a photoelectron current from the probe to other conducting elements (including the stub) at the zero probe potential.

3.2. Stray Photoelectron Currents

[29] When the sensor consists of multiple conductor elements, the conductor elements are electrically coupled to each other via a stray current I_{stray}. We confirmed the presence of a strong coupling for $\phi_{pr} \geq 0$, as shown in Figure 4b. In contrast, this electric coupling is negligibly weak for $\phi_{pr} < 0$.

[30] The magnitude of $I_{pr\rightarrow o}$ increases rapidly as the potential increases to $\phi_{pr}/\phi_{ph} \sim 5$, while it decreases gradually above this potential. $I_{o\rightarrow pr}$ increases consistently with increasing potential for $\phi_{pr}/\phi_{ph} \geq 0$. Consequently, the curve for I_{stray}, which is the sum of $I_{pr\rightarrow o}$ and $I_{o\rightarrow pr}$, exhibits peculiar behavior; specifically, the sign of I_{stray} is reversed at $\phi_{pr}/\phi_{ph} \sim 17$.

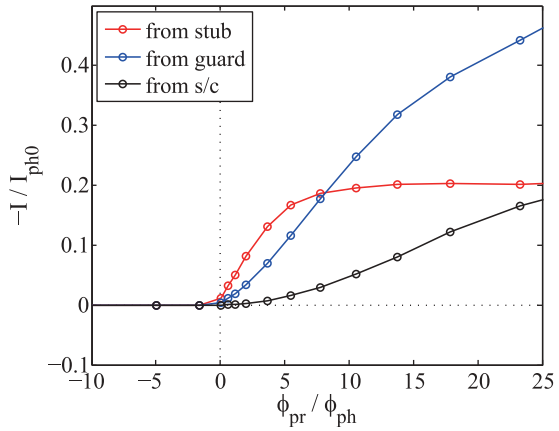

Figure 5. Stray photoelectron currents from the stub (red line), guard (blue line), and the spacecraft body (including the boom) (black line) as a function of ϕ_{pr}.

[31] We are particularly interested in the nature of $I_{o\rightarrow pr}$ because the magnitude of $I_{o\rightarrow pr}$ should be sensitive to small variations in the attitude of the spacecraft in the sunlight direction, the operational settings of the guard and stub potentials, and the geometric design of the instrument. To clarify the composition of $I_{o\rightarrow pr}$, we plot stray photoelectron currents originating from the stub, guard, and spacecraft body (including the boom) separately in Figure 5.

[32] Figure 5 clearly shows that all the stray current components increase with increasing probe potential. The stray current from the stub increases rapidly in $0 \le \phi_{pr}/\phi_{ph} < 5$. In $\phi_{pr}/\phi_{ph} \ge 5$, the current from the stub is nearly saturated. The currents from the guard and the spacecraft body show relatively moderate increases at low probe potentials. However, these currents increase consistently without saturating.

[33] To better understand the characteristic signatures of the current–voltage curves, we study the detailed behavior of photoelectrons for each of their origins, i.e., the stub, guard, and spacecraft body. In the analysis, we compare the simulation results for ϕ_{pr}/ϕ_{ph} = 1.1 and 11, which correspond to probe working points of $I_{bias} = 0.9I_{bias0}$ and I_{bias} = 0, respectively. Here, I_{bias0} is the bias current that produces ϕ_{pr} = 0.

3.2.1. Photoelectron Current From Stub

[34] Figure 6 shows plots of the density, flow vector, and potential near the puck and the probe. In the density and flow vector plots, only the contribution of photoelectrons from the stub is plotted. The density plots in Figures 6a and

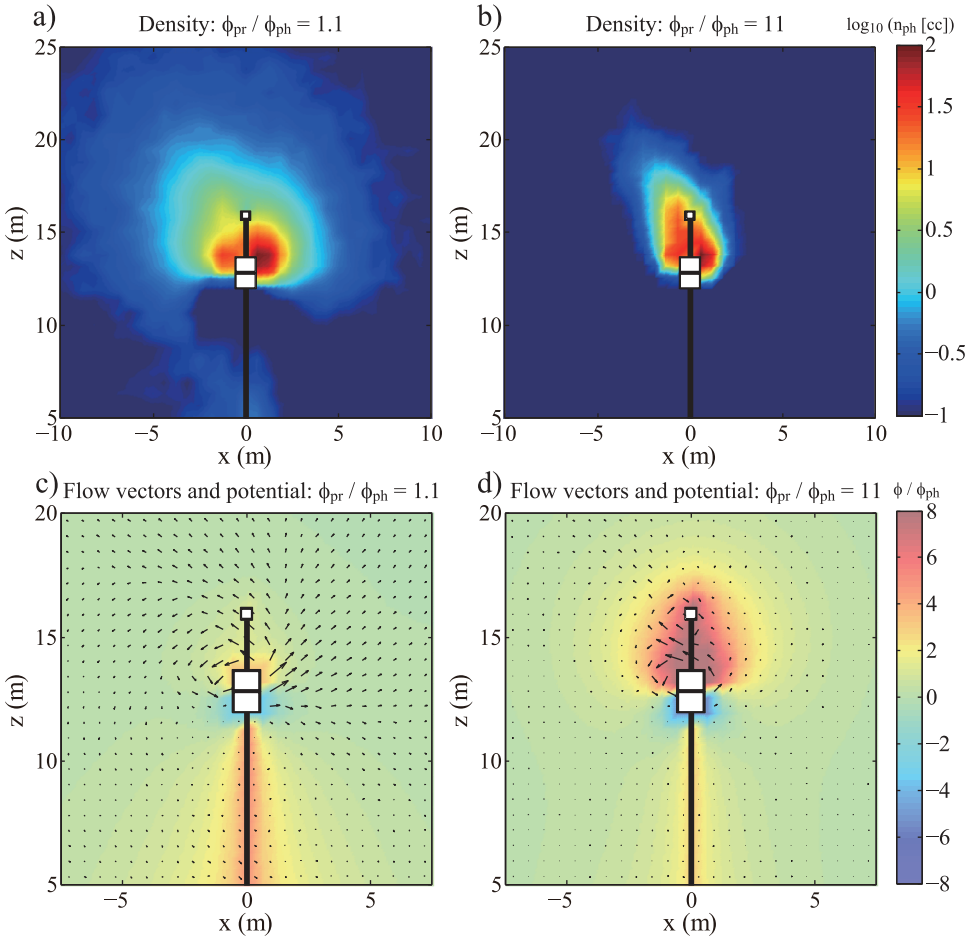

Figure 6. Plots of the (a and b) density and (c and d) flow vectors of photoelectrons from the stub. Figures 6a and 6c correspond to the probe operation point ϕ_{pr}/ϕ_{ph} = 1.1, while Figures 6b and 6d to ϕ_{pr}/ϕ_{ph} = 11. Photoelectron flow vectors are superimposed onto the background color maps showing the electric potential distributions.

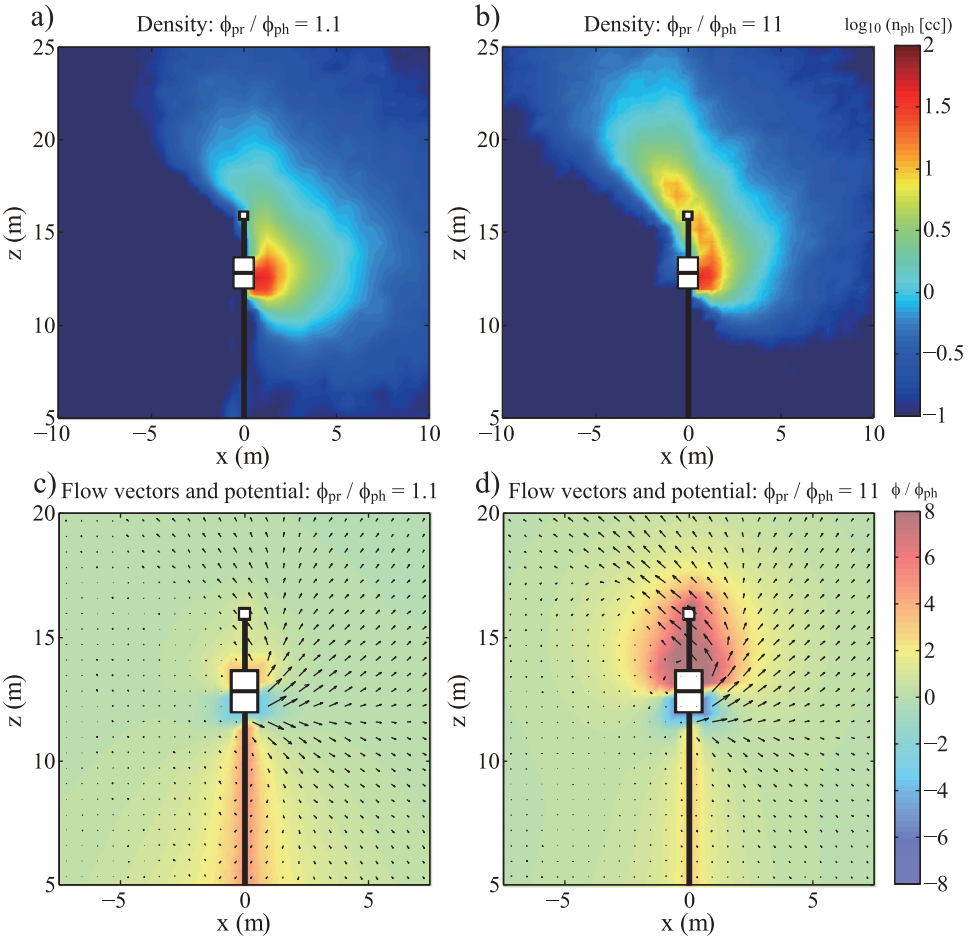

Figure 7. Plots of the (a and b) density and (c and d) flow vectors of photoelectrons from the guard. Figures 7a and 7c correspond to the probe operation point ϕ_{pr}/ϕ_{ph} = 1.1, while Figures 7b and 7d to ϕ_{pr}/ϕ_{ph} = 11. Photoelectron flow vectors are superimposed onto the background color maps showing the electric potential distributions.

6b show that the photoelectrons are confined near the stub and the probe for both probe working points. In comparison of the results for the two probe working points, the photoelectron confinement is insufficient for ϕ_{pr}/ϕ_{ph} = 1.1, whereas photoelectrons are strongly confined in a very small region for ϕ_{pr}/ϕ_{ph} = 11. This latter confinement obviously promotes photoelectron absorption by the probe, which generates a large stray current between the stub and the probe. Actually, the photoelectron densities at the probe position are 2.3 times higher for ϕ_{pr}/ϕ_{ph} = 11 than for ϕ_{pr}/ϕ_{ph} = 1.1 under the present parameter settings.

[35] The photoelectron dynamics associated with the confinement are depicted by photoelectron flow vectors plotted with background contour maps for the electric potential in Figures 6c and 6d. Escaping photoelectrons from the stub are strongly repelled by the potential barrier created by the guard that has a large negative potential. The flow of the deflected photoelectrons is directed toward the probe and a large proportion of the photoelectrons approach the probe. The figures also show that the stub and probe with positive potentials with respect to the background plasma form a potential well for the photoelectrons. This potential well prevents the photoelectrons from escaping from the vicinity of the stub and probe, particularly when ϕ_{pr}/ϕ_{ph} = 11.

[36] The shape of the stray current curve shown in Figure 5 can be explained in terms of the above results. The efficiency of the photoelectron confinement is a function of the probe-to-plasma potential and increases with increasing probe potential in the range $0 \le \phi_{pr}/\phi_{ph} < 5$, leading to a steep increase in the stray current magnitude. Once effective confinement has been achieved, almost all emitted photoelectrons should be collected by either the probe (with the thin sensor wire) or the stub. In the present simulations, the total photoelectron current emitted from the stub is $\sim 3I_{ph0}$. This indicates that 0.2/3∼7% of the total current is collected by the probe, and the remaining is recollected by the stub itself. A primary factor that can influence this rate 7% is the potential difference between the stub and the probe. However, in the current biasing scheme, the stub potential is strictly fixed to $+2\phi_{ph}$ relative to the probe potential regardless of the probe working point. Consequently, the rate of photoelectrons collected by the probe and the resulting current magnitude become almost constant above ϕ_{pr}/ϕ_{ph} = 5.

3.2.2. Photoelectron Current From Guard

[37] Figure 7 depicts the distribution and dynamics of photoelectrons from the guard; it uses the same format as Figure 6. Figures 7c and 7d show that photoelectrons

emitted from the guard surface expand radially from the guard position. Since the negatively charged guard forms a potential hump for electrons, emitted photoelectrons are immediately accelerated away from the guard. Although some of these photoelectrons are trapped by the potential well produced by the probe and the stub, many of them eventually escape from the influence sphere of the probe and stub potentials. The escape rate of such photoelectrons is greater for ϕ_{pr}/ϕ_{ph} = 1.1 than for ϕ_{pr}/ϕ_{ph} = 11.

[38] The photoelectron dynamics described above are clearly reflected in the photoelectron distributions shown in Figures 7a and 7b. The photoelectron cloud next to the guard surface extends toward the probe. However, because of insufficient deflection of the photoelectron orbits, the core of the photoelectron distribution does not include the probe location for ϕ_{pr}/ϕ_{ph} = 1.1. In contrast, probe is totally enclosed by the extended photoelectron cloud for ϕ_{pr}/ϕ_{ph} = 11. As a result, the photoelectron densities at the probe position are found to be 7.9 times higher for ϕ_{pr}/ϕ_{ph} = 11 than for ϕ_{pr}/ϕ_{ph} = 1.1, and this difference is stronger than that observed for the photoelectrons from the stub.

[39] In Figure 5, the stray current from the guard increases gradually without saturating, even at high potentials. This behavior is in stark contrast to that of the current from the stub. In comparison with the photoelectrons from the stub, only a small portion of the photoelectrons from the guard can be captured by the potential well around the probe as can be seen in Figures 7c and 7d. Although the proportion of captured photoelectrons should increase with increasing ϕ_{pr}, a complete trapping by the potential well cannot be achieved for the photoelectrons from the guard in the potential range in consideration, whereas almost all photoelectrons from the stub are trapped by the potential well sufficiently within the potential range. This behavioral difference is reflected in the shapes of the characteristic curves for the stray currents from the stub and guard.

3.2.3. Photoelectron Current From Spacecraft Body

[40] Finally, we consider photoelectrons emitted by the spacecraft body and the boom. As for the other two photoelectron components, we plot the photoelectron density distributions for ϕ_{pr}/ϕ_{ph} = 1.1 and 11 in Figures 8a and 8b, respectively. The difference between the two cases is mainly observed in the region beyond the guard position. For ϕ_{pr}/ϕ_{ph} = 1.1, the photoelectron cloud is effectively blocked at the guard. This results in a relatively low photoelectron density 0.07 cc^{-1} at the probe, which is just 0.2% of the averaged photoelectron density on the boom surface. In contrast, such a guard effect is less significant for ϕ_{pr}/ϕ_{ph} = 11, so that the photoelectron cloud extends beyond the guard position, giving density at the probe of 6% of the averaged photoelectron density on the boom surface.

[41] Because a stray current between the spacecraft and the probe consists of only a small fraction of a total photoelectron flux from the spacecraft body, it is not helpful to plot photoelectron flow maps such as those in Figures 6 and 7. Instead, Figures 8c and 8d show representative examples of trajectories of photoelectrons that contribute to the stray current. To obtain these plots, we initialized $\sim 10^4$ test photoelectrons with various velocities, ejection angles, and starting positions on the spacecraft and boom surfaces in addition to macro-particles used for the PIC simulations. We then examined the trajectories of the test electrons in the *x-z* plane. The initial kinetic energies of the test electrons range from 0 to $10\phi_{ph}$. The plots show only photoelectrons absorbed by the probe. In the plots, the colors of the trajectories indicate the initial photoelectron kinetic energy (see the rightmost color bar).

[42] For ϕ_{pr}/ϕ_{ph} = 1.1, most of trapped photoelectrons originate from the spacecraft body, whereas photoelectrons emitted from both the spacecraft body and the boom are trapped for ϕ_{pr}/ϕ_{ph} = 11. Some of the photoelectrons are deflected by the guard, but they are subsequently attracted by the potential well created by the probe charged positively. In Figure 8d, the initial positions of the trapped photoelectrons are distributed on the boom surface in the ranges of *z*-coordinate from z = 2.5 m to 4 m and from z = 5.5 m to 9 m. The lower-energy portion of trapped photoelectrons mainly originates from boom surface segments relatively close to the guard. However, photoelectrons emitted from segments much closer to the guard are completely repelled by the guard potential and do not approach the probe position.

[43] The energy range of photoelectrons trapped by the probe decreases with increasing ϕ_{pr}, as the comparison for ϕ_{pr}/ϕ_{ph} = 1.1 and 11 shows. Specifically, trapped photoelectrons have energies in the range $9.2e\phi_{ph}$ to $10e\phi_{ph}$ for ϕ_{pr}/ϕ_{ph} = 1.1 and in the range $3.5e\phi_{ph}$ to $7e\phi_{ph}$ for ϕ_{pr}/ϕ_{ph} = 11.

[44] The absolute number of lower-energy photoelectrons is generally much greater than that of high-energy photoelectrons. Hence, the probe can trap more photoelectrons when the energy range that can be trapped is lower. In light of this, the result described in the previous paragraph well explains the gradual increase in the stray current with increasing ϕ_{pr} shown in Figure 5.

3.2.4. Practical Implications of the Results

[45] In the preceding subsections, we studied the photoelectron distribution and dynamics focusing two probe working points ϕ_{pr}/ϕ_{ph} = 1.1 and 11. Among them, the working point ϕ_{pr}/ϕ_{ph} = 1.1 corresponds to a more practical situation in actual use of electric field sensors simulated here. Generally, electric field sensors should be operated near the background plasma potential with a small offset potential, which prevents the probes from falling into an unstable negative potential regime [e.g., *Blomberg et al.*, 2006]. Because the offset potential is normally less than or comparable to ϕ_{ph}, the working point ϕ_{pr}/ϕ_{ph} = 1.1 is considered to be an appropriate selection.

[46] The merit of the working point choice near the plasma potential is generally explained in terms of a better stability of the probe potential against fluctuations of incoming plasma and photoelectron currents (i.e., a lower probe-to-plasma impedance [e.g., *Gustafsson et al.*, 1997]). In addition to this merit, such a working point is found to be useful also for minimizing the stray current magnitude originating from the other conducting elements. That is a quite natural result for photoelectrons coming from the spacecraft body, because the spacecraft potential is always higher than the background potential in tenuous plasma environments. More importantly, we learn from the present simulations that such a working point can also reduce the photoelectron currents coming from the stub and guard electrodes.

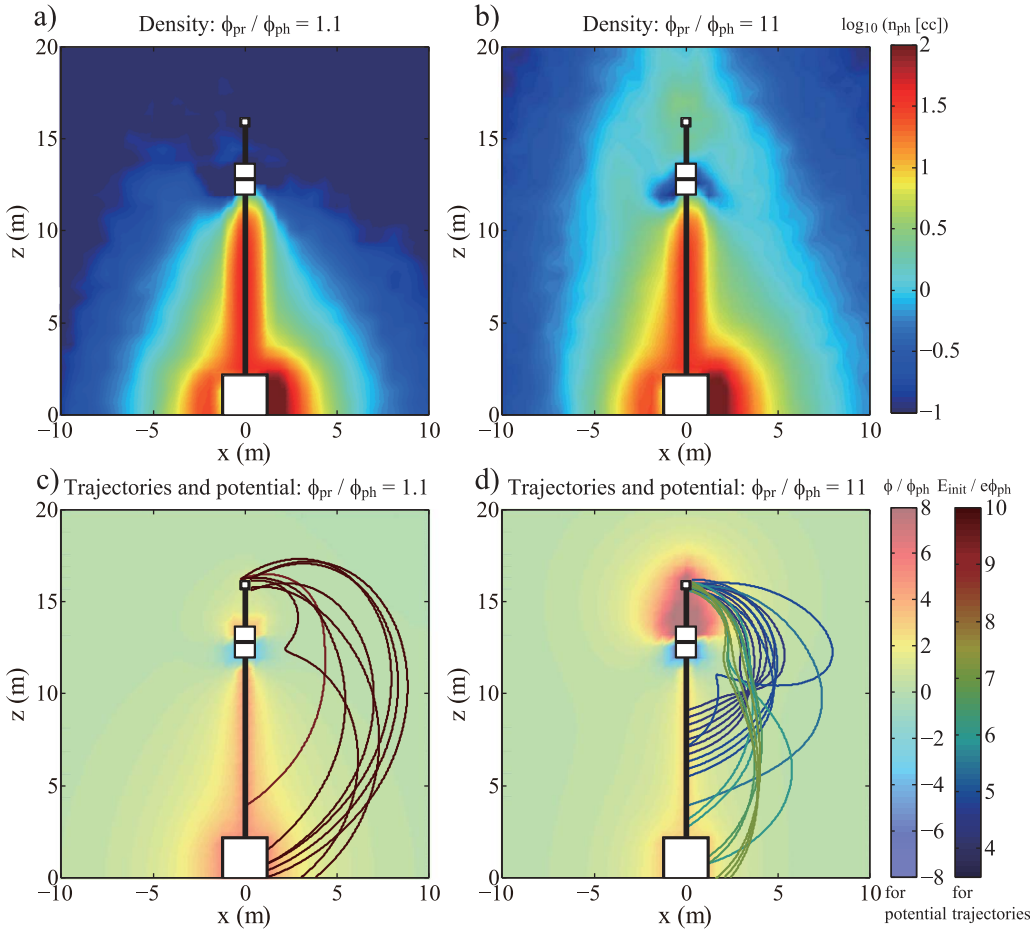

Figure 8. Plots of the (a and b) density and (c and d) trajectories of photoelectrons from the spacecraft and boom. Figures 8a and 8c correspond to the probe operation point ϕ_{pr}/ϕ_{ph} = 1.1, while Figures 8b and 8d to ϕ_{pr}/ϕ_{ph} = 11. In the bottom panels, the trajectories of photoelectrons absorbed by the probe are plotted with background color map showing electric potential distribution. The plot was obtained by calculating the dynamics of about $\sim 10^4$ test particles with various initial energies and ejection angles (see main text for details). The colors of the trajectory lines indicate the initial kinetic energies E_{init} of the photoelectrons (see rightmost color bar).

3.3. Effect of Guard Electrode

[47] *Miyake et al.* [2011] studied in detail the benefit of using the guard electrode against photoelectrons coming from the spacecraft, and the analysis was done for a single probe working point. Here, we extend the analysis to consider the effect of the guard on the current–voltage characteristics of the probe. We also consider effects of the guard on the photoelectrons from the stub and guard. To determine the effect of the guard, we have changed the guard-to-spacecraft and stub-to-probe potentials to zero and redone a series of the simulations. These new simulations can reproduce a situation without any guard electrode operation. Figure 9 compares current–voltage curves obtained with and without the guard electrode operation.

[48] Figure 9a shows the curve for the net current $-I_p$. The effect of the guard is observed in the probe potential range $\phi_{pr} \geq 0$. For $0 \leq \phi_{pr}/\phi_{ph} < 5$, the current increases more gradually when the guard is off compared to when it is on, although the difference between the two cases is relatively small. The situation is reversed for $\phi_{pr}/\phi_{ph} \geq 5$; i.e., the current increases more rapidly when the guard is off than when it is on. In this potential range, there is a large difference seen between the two cases.

[49] Although not shown here, little difference in I_{ph} and I_e was observed for the two cases; thus, the above result originates mainly from the change in the characteristics of I_{stray}. Figures 9b–9d show plots of the stray currents due to photoelectrons from the stub, guard, and spacecraft body (including the boom), respectively. The main purpose of introducing the guard is to minimize the photoelectron current from the spacecraft body and boom. Figure 9d shows that this aim was realized. The guard electrode reduced the increase rate in the photoelectron current from the spacecraft body and boom. Particularly, in a practical probe working potential range around ϕ_{pr}/ϕ_{ph} = 1, we confirm the photoelectron current reduction of greater than 90%.

[50] The photoelectron current from the guard exhibits a more complex tendency as shown in Figure 9c. The current

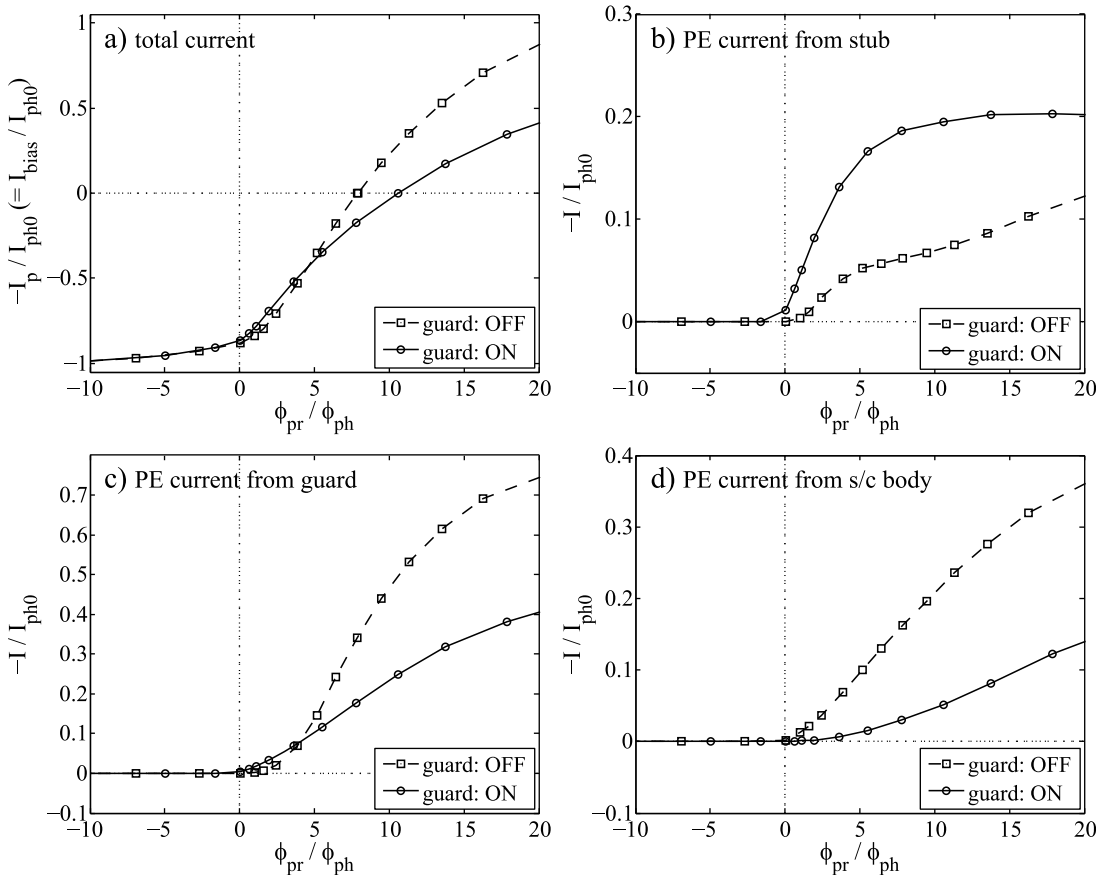

Figure 9. Comparison of stray photoelectron current magnitudes obtained with and without a photoelectron guard electrode operation. (a) Total current–voltage curve of electric field sensor. Stray photoelectron currents from (b) stub, (c) guard, and (d) spacecraft body.

is slightly smaller when the guard is off than when it is on up to $\phi_{pr}/\phi_{ph} = 4$; for higher probe potentials, the current for when the guard is off increases abruptly and exceeds that for the guard is on. Among these two regimes, the guard effect seen below $\phi_{pr}/\phi_{ph} = 4$ should receive more attention in a practical sense, although the effect is relatively small. The result can be explained by considering the relation between guard and probe potentials. When the guard is off, the guard potential is equal to the spacecraft potential ϕ_{sc}. As a result, the probe potential is lower than the guard potential in a range of $\phi_{pr} < \phi_{sc}$. Meanwhile, when the guard is on, the probe potential is consistently higher than the guard potential even for $\phi_{pr} < \phi_{sc}$. Consequently, more photoelectrons from the guard flow to the probe when the guard is on.

[51] Finally, the photoelectron current from the stub is enhanced consistently by the guard operation, as Figure 9b clearly shows. The result is difficult to explain by merely considering the relation between the stub and probe potentials, because the stub potential, which is higher than the probe potential when the guard is on, should produce the opposite to the observed result. To interpret the result, it is necessary to consider the relation between the stub and guard potentials. When the guard is on, the potential barrier generated by the negatively charged guard strongly repels the photoelectrons and directs them toward the probe, which enhances the photoelectron current to the probe. This is confirmed by Figures 6c and 6d.

[52] When the guard is off, this repulsive effect is greatly weakened or even not observed since the guard potential is positive. Specifically, the guard potential is higher than the stub potential for $\phi_{pr}/\phi_{ph} < 5$ and thus the photoelectrons from the stub are rather attracted than repelled by the guard. For $\phi_{pr}/\phi_{ph} \geq 5$, the guard potential becomes lower than the stub potential even when the guard is off, and the photoelectrons start to be repelled by the guard. This also provides a reasonable interpretation for the gradual increase in the current above $\phi_{pr}/\phi_{ph} = 5$ when the guard is off.

[53] In summary, the guard has the positive effect of reducing the stray currents from the spacecraft body. On the other hand, the guard does not reduce and may even enhance the stray currents from the stub and guard in a practically used range of the probe potential. This finding was not noted in previous studies. This effect could be minimized by employing another approach; for example, by making the puck dimensions as small as possible to minimize the photoelectron flux. In practice, the puck dimensions are generally much smaller than those employed in the present numerical model. Hence, the stray currents from the stub and the guard are overestimated in the present analysis compared

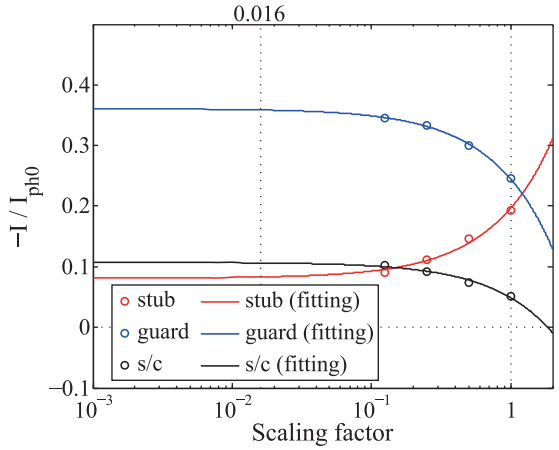

Figure 10. Dependence of the stray photoelectron currents on variation of the potential structure associated with variations in the dimensions of the sensor and boom wires, stub, and guard. The horizontal axis represents the factor of effective radii of the sensor and boom wires, stub, and guard, (unity corresponds to the radii of the original model). The red, blue, and black circles represent the results for the photoelectron currents from the stub, guard, and spacecraft obtained by simulations that mimicked the reduced effective radii of the sensor and boom wires and the puck (see main text). The solid lines are depicted by fitting based on the linear least squares method (they appear as curves because the horizontal axis has a logarithmic scale).

with those in reality. This aspect is discussed in the following section.

4. Discussion

4.1. Scaling Analysis of Photoelectron Currents

[54] A major difficulty that is always encountered when using the self-consistent PIC approach is the modeling of fine structures of practical sensors. An extreme example is the radii of boom and sensor wires (typically 0.1–1 mm), which are too small compared with a spatial scale of the Debye shielding by photoelectrons. A less extreme example is the probe radius and puck dimensions, which are of the order of cm. Nonetheless they lie within the sub-Debye scale of photoelectrons.

[55] Since it is difficult to overcome this problem in the self-consistent approach, we are forced to simulate the sensor model, some parts of which are artificially large. This enlargement leads to overestimation of the absolute magnitudes of photoelectrons currents relative to those for practical sensors. In this section, we attempt to approximately estimate the degree of the overestimation.

[56] Sensor enlargement mainly affects: 1. the photoelectron-collecting surface area of the probe, 2. the photoemitting surface areas of the puck and boom, and 3. the potential structure created around the sensor. Of these, the first factor affects both photoelectron and background plasma collection by the same factor. Thus, it should have a minor effect on the relative importance of the stray current with respect to the other current components.

[57] The second factor greatly affects the magnitudes of the photoelectron currents from the stub, guard, and boom. Fortunately, it can be easily estimated by considering scaling of photoemitting surface areas for the puck and the boom because the photoelectron fluxes are simply proportional to the areas. The photoemitting surface area of the puck is 2.5 m^2 in the simulation model, whereas is of the order of 10^{-3} m^2 in practical sensors. Thus, the photoelectron fluxes from the guard and stub are overestimated by a factor of approximately 10^3. The boom radii used in the simulation and practical sensors are 6.3 cm and ~1 mm, respectively. Consequently, the photoelectron flux from the boom is overestimated by a factor of 10^1 in the simulation.

[58] It is more difficult to assess the third factor. The potential structure around the sensor is complex (as shown in the previous section) due to there being multiple conducting elements with various potentials. The influence of such a potential structure on photoelectron orbits is thus very difficult to estimate analytically. We thus need to perform additional numerical evaluations.

[59] To mimic potential structures produced by smaller sensor dimensions, we introduce a quasi-analytical model and make some assumptions in the simulations. The fundamental assumption is that the electric potentials near the thin wire elements and the puck follow simple analytical solutions for the potentials generated by cylindrical and spherical conductors in vacuum, respectively. Then, in the simulations, we fixed the potentials of grid points adjacent to the center of the conducting elements to the analytical values. Although this assumption completely excludes Debye shielding effects due to surrounding plasma and photoelectrons, this should cause only minor errors provided the adjacent grid points are located sufficiently within the Debye sphere centered on the conducting elements. Another source of error is that we neglect the presence of multiple conductors in the analytical solutions. Since this may result in larger errors than the previous one, we limit the use of the present numerical evaluation for approximate estimations.

[60] We performed three simulations to imitate potential structures with reduced effective radii for the sensor and boom wires and the puck by factors of 1/2, 1/4, and 1/8 from the original model, respectively. We chose a probe-working point of $\phi_{pr}/\phi_{ph} \sim 11$ for the simulations. Moreover, to focus on the impact of the potential structure, we kept the photoemitting and plasma-collecting surface areas the same as the original model. Figure 10 shows the variation in the stray photoelectron currents obtained by the simulations. Since we found the currents depend almost linearly on the reduced radii, we fitted the plots using the linear least squares method. (Note that the linear fitted plots appear as curves in the figure because the horizontal axis has a logarithmic scale).

[61] The results clearly show that the change in the potential structure caused by the reduced effective radii increases the photoelectron currents from the guard and the spacecraft body. In contrast, this change reduces the photoelectron current from the stub. This trend is consistent with that observed when we disable the guard, as discussed in the previous section.

[62] We estimated the stray currents for practical sensor dimensions by extrapolating the results. Practical sensors

have a wire radius and puck dimensions of ~1 mm and a few cm, respectively. These dimensions correspond to a scaling factor of $\sim 1.6 \times 10^{-2}$ in Figure 10. The photoelectron current magnitudes from the stub, guard, and spacecraft body should be 0.43, 1.5, and 2.1 times the original magnitudes, respectively. In addition to the influence of the potential structure, we also considered the photoemitting surface areas of the puck and the boom in a practical sensor, which has been already discussed earlier. As a final result, the magnitudes of the stray photoelectron currents from the stub and the guard are of the order $10^{-4}\ I_{ph0}$, whereas that from the spacecraft body is of the order $10^{-1}\ I_{ph0}$.

[63] This scaling analysis based on the dimensions of a practical sensor suggests that the photoelectron current from the spacecraft body is most important, while the photoelectron currents from the stub and the guard are secondary factors. This result essentially validates the accepted design of the photoelectron guard electrode, the primary purpose of which is to repel photoelectrons from the spacecraft body.

[64] On the other hand, this situation will change in some specific environments such as extremely tenuous plasmas. In such an environment, a large positive spacecraft potential of a few tens of V will strongly attract photoelectrons from the spacecraft and thus the absolute magnitude of the stray photoelectron current from the spacecraft body will be lower than in other environments. In such a situation, photoelectrons from the puck will be more significant than in other environments. The characteristics of photoelectrons from the stub and the guard determined in this study will be helpful for such potential problems caused by photoelectrons from the puck.

4.2. Verification of Excluding Static Magnetic Field

[65] Although the presence of the static magnetic field is a potential factor affecting the photoelectron trajectories, we assume that its practical impact is small in the plasma environment in consideration. In order to verify this assumption, we have performed additional simulations including the magnetic field of 50 nT aligned with *x*-, *y*-, or *z*-axes. Consequently, the magnitudes of the photoelectron currents are changed only by a factor of 0.1% of I_{ph0} at maximum by the magnetic field inclusion. The orientation of the magnetic field also has no practical influence on the current magnitude. The observed difference of $10^{-3}\ I_{ph0}$ is a rather minor factor and is negligible in the present study. Because typical magnetic field strength is comparable to or even smaller than 50 nT in outer magnetospheric environments, we conclude that excluding a magnetic field in the present analysis is a sound assumption.

[66] The above result is understandable by considering the spatial scale of the sensor relative to a typical photoelectron gyroradius (i.e., ~70 m). When a photoelectron traveling distance is smaller than its gyroradius, the photoelectron should behave as if it were not magnetized. Note that this regime is also valid even for the Cluster instrument located in outer magnetospheric environments, because the distance 42.5 m between the spacecraft surface and the probe is usually smaller than the typical photoelectron gyroradius.

[67] Although the magnetic field is negligible in the present situation, the magnetic field effects on the photoelectron trajectories are of general interest. We thus have performed additional simulations having the magnetic field of 500 nT. In this case, the magnitude of a photoelectron current coming from the spacecraft is considerably altered by the magnetic field inclusion. More specifically, the photoelectron current shows a minimum value when the magnetic field is applied perpendicularly to the sensor direction. For photoelectron currents from the stub and guard, such an appreciable modulation due to the magnetic field is not observed. This is due to the short traveling distance of the photoelectrons, which is sufficiently shorter than the photoelectron gyroradius. The additional simulations suggest that the magnetic field effects should receive special attention in the inner magnetospheric environments. Such a domain is out of the scope of the present study and should be examined in the future work.

5. Conclusions

[68] In tenuous space plasma environments, large photoelectron currents from the conducting surfaces of a spacecraft modify the electrical properties of double-probe electric field sensors. We performed full-particle simulations to analyze the current–voltage characteristics of an electric field sensor surrounded by a dense photoelectron cloud. The numerical model used in this study is based on the recent sensor designed for the BepiColombo/MMO mission. We employ a plasma particle model that allows full information to be obtained about photoelectron currents by tracing the orbits of particles.

[69] Our numerical study reveals that the sensor current–voltage characteristics are substantially affected by the stray photoelectron currents flowing between the probe and other conducting elements such as the stub, the guard, and the spacecraft body, whenever the sensor probe has a positive potential. One of the most significant knowledge obtained in the present analysis is that the stray photoelectron currents increases with increasing probe potential regardless of their origins in a probe potential range near the plasma potential, which is normally used in electric field measurements. This result suggests that not only the spacecraft-originating photoelectron current but also the puck-originating photoelectron current can be reduced by selecting the probe working potential as close as possible to the plasma potential. The present simulations also reveal the photoelectron current behavior at higher probe potentials. The stray photoelectron currents from the guard and the spacecraft body increase monotonically even in this potential range. Meanwhile, the magnitude of the stray current from the stub saturates at a probe potential close to the spacecraft potential. In contrast with these unknown outcomes, the behavior of the background plasma current agrees well with the conventional theory.

[70] Due to the presence of the photoelectron guard electrode, only a small fraction of the photoelectrons from the spacecraft and the boom approach the probe. The minimum photoelectron energy required to approach the probe decreases with increasing probe potential. This dependence can be well described by photoelectron orbital analysis; the photoelectrons are deflected by the guard potential but are subsequently attracted by the potential well created by the probe. Also, this potential well acts more directly on the photoelectrons emitted by the stub and guard adjacent to the probe. In particular, photoelectrons from the stub generate a very clear flow toward the probe due to photoelectron repulsion by the guard potential.

[71] A major limitation of the numerical model is that it does not employ realistic sensor dimensions; rather it uses artificially large dimensions to enable simulations to be performed with limited computational resources. An approximate scaling evaluation strongly suggests that the dominant component of the stray photoelectron current is that coming from the spacecraft body. Note that the ratio of the stray current to the total emission is smallest for photoelectrons from the spacecraft body. Nevertheless, the stray current from the spacecraft is most important because the photoemitting surface area of the spacecraft body is considerably greater than those of the other elements.

[72] We also confirmed that the photoelectron guard electrode has a positive effect in that it suppresses the magnitudes of the stray photoelectron current from the spacecraft body. This is a well-known effect of the guard electrode. The present study also revealed that the guard electrode operation enhanced the stray photoelectron currents from the stub and guard, which has not been noted in previous studies. This anomalous behavior should have a minor effect on the sensor properties, except for in extremely tenuous plasma environments. In extremely tenuous plasmas, confinement of photoelectrons from the spacecraft by the high spacecraft potential enhances the relative importance of photoelectrons from the stub and guard. In such a case, the side effect of the guard operation will require more attention.

[73] This paper did not examine the dependence of the stray current on the sunlight incident angle, which is important for probes in spin planes. The magnitudes of the photoelectron currents from the guard and spacecraft are expected to be affected by this angle because the photoelectron orbits are an essential factor in determining the current magnitudes. The magnitude of the photoelectron current from the stub should be less sensitive to the sunlight incident angle because the photoelectrons will be highly confined near the stub and the probe, irrespective of the photoelectron ejection direction. Further analysis may provide more insight into this.

[74] A remaining topic for investigation is the effect of the boom length on the photoelectron current. In particular, spin-axial electric field sensors should be shorter than the present model for mechanical reasons. The enhanced influence of photoelectrons from the spacecraft on the sensor should be evaluated in future studies.

[75] In conclusion, we have studied the photoelectron current around an electric field sensor by subdividing the current components based on their origin. This approach reveals a complex mechanism of electric coupling between the sensor probe and the other conducting elements in association with electric potential structures around the spacecraft. We consider that the information obtained will be helpful for optimizing the designs of photoelectron guard electrodes and electric field sensors.

[76] **Acknowledgments.** The authors would like to thank L. Åhlén for helpful comments on the proposed numerical model of the instrument. The computations in the present study were performed using the KDK system of Research Institute for Sustainable Humanosphere (RISH) and the Fujitsu HX600 Cluster of Academic Center for Computing and Media Studies (ACCMS) at Kyoto University.

[77] Masaki Fujimoto thanks the reviewers for their assistance in evaluating this paper.

References

Birdsall, C. K., and A. B. Langdon (1985), *Plasma Physics via Computer Simulation*, McGraw-Hill, New York.

Blomberg, L. G., et al. (2006), MEFISTO—An electric field instrument for BepiColombo/MMO, *Adv. Space Res.*, *38*, 672–679, doi:10.1016/j.asr.2005.05.032.

Bonnell, J. W., F. S. Mozer, G. T. Delory, A. J. Hull, R. E. Ergun, C. M. Cully, V. Angelopoulos, and P. R. Harvey (2008), The Electric Field Instrument (EFI) for THEMIS, *Space Sci. Rev.*, *141*, 303–341, doi:10.1007/s11214-008-9469-2.

Cartwright, K. L., J. P. Verboncoeur, and C. K. Birdsall (2000), Loading and injection of Maxwellian distributions in particle simulations, *J. Comput. Phys.*, *162*, 483–613, doi:10.1006/jcph.2000.6549.

Cully, C. M., R. E. Ergun, and A. I. Eriksson (2007), Electrostatic structure around spacecraft in tenuous plasma, *J. Geophys. Res.*, *112*, A09211, doi:10.1029/2007JA012269.

Fahleson, U. (1967), Theory of electric field measurements conducted in the magnetosphere with electric probes, *Space Sci. Rev.*, *7*, 238–262.

Gurnett, D. A. (1998), Principles of space plasma wave instrument design, in *Measurement Techniques in Space Plasmas: Fields*, *Geophys. Monogr. Ser.*, vol. 103, edited by R. F. Pfaff et al., pp. 121–136, AGU, Washington, D. C.

Gustafsson, G., et al. (1997), The electric field and wave experiment for the Cluster mission, *Space Sci. Rev.*, *79*, 137–156, doi:10.1023/A:1004975108657.

Gustafsson, G., et al. (2001), First results of electric field and density observations by Cluster EFW based on initial months of operation, *Ann. Geophys.*, *19*, 1219–1241.

Hershkowitz, N. (1989), How Langmuir probes work, in *Plasma Diagnostics*, vol. 1, edited by O. Auciello and D. L. Flamm, pp. 113–184, Academic, San Diego, Calif.

Lai, S. T. (2011), *Fundamentals of Spacecraft Charging*, Princeton Univ. Press, Princeton, N. J.

Miyake, Y., and H. Usui (2009), New electromagnetic particle simulation code for the analysis of spacecraft-plasma interactions, *Phys. Plasmas*, *16*, 062904, doi:10.1063/1.3147922.

Miyake, Y., H. Usui, H. Kojima, Y. Omura, and H. Matsumoto (2008), Electromagnetic particle-in-cell simulation on the impedance of a dipole antenna surrounded by an ion sheath, *Radio Sci.*, *43*, RS3004, doi:10.1029/2007RS003707.

Miyake, Y., H. Usui, and H. Kojima (2011), Effects of the guard electrode on the photoelectron distribution around an electric field sensor, *J. Geophys. Res.*, *116*, A05211, doi:10.1029/2010JA015600.

Mott-Smith, H. M., and I. Langmuir (1926), The theory of collectors in gaseous discharges, *Phys. Rev.*, *28*, 727–763, doi:10.1103/PhysRev.28.727.

Mozer, F. S., and P. Bruston (1967), Electric field measurements in the auroral ionosphere, *J. Geophys. Res.*, *72*, 1109–1114, doi:10.1029/JZ072i003p01109.

Mozer, F. S., C. W. Carlson, M. K. Hudson, R. B. Torbert, B. Parady, J. Yatteau, and M. C. Kelley (1976), Observations of paired electrostatic shocks in the polar magnetosphere, *Phys. Rev. Lett.*, *38*, 292–295, doi:10.1103/PhysRevLett.38.292.

Nakashima, H. (2008), T2K open supercomputer: Inter-university and inter-disciplinary collaboration on the new generation supercomputer, in *Proceedings of the International Conference on Informatics Education and Research for Knowledge-Circulating Society*, pp. 137–142, Inst. of Elect. and Electron. Eng., Piscataway, N. J., doi:10.1109/ICKS.2008.6.

Nakashima, H., Y. Miyake, Y. Omura, and H. Usui (2009), OhHelp: a scalable domain-decomposing dynamic load balancing for particle-in-cell simulations, in *Proceedings of the 23rd International Conference on Supercomputing*, pp. 90–99, Assoc. for Comput. Mach., New York, doi:10.1145/1542275.1542293.

Pedersen, A., C. A. Cattell, C.-G. Fälthammar, V. Formisano, P.-A. Lindqvist, F. Mozer, and R. Torbert (1984), Quasistatic electric field measurements with spherical double probes on the GEOS and ISEE satellites, *Space Sci. Rev.*, *37*, 269–312, doi:10.1007/BF00226365.

Pedersen, A., F. Mozer, and G. Gustafsson (1998), Electric field measurements in a tenuous plasma with spherical double probes, in *Measurement Techniques in Space Plasmas: Fields*, *Geophys. Monogr. Ser.*, vol. 103, edited by R. F. Pfaff et al., pp. 1–12, AGU, Washington, D. C.

Pedersen, A., et al. (2008), Electron density estimations derived from spacecraft potential measurements on Cluster in tenuous plasma regions, *J. Geophys. Res.*, *113*, A07S33, doi:10.1029/2007JA012636.

Tsuruda, K., H. Hayakawa, M. Nakamura, T. Okada, A. Matsuoka, F. S. Mozer, R. Schmidt (1994), Electric field measurements on the GEOTAIL satellite, *J. Geomag. Geoelectr.*, *46*, 693–711.